

To appear in the Astrophysical Journal

Nonlinear Force-Free Extrapolation of the Coronal Magnetic Field Based on the MHD Relaxation Method

S. Inoue

*School of Space Research, Kyung Hee University, Yongin, Gyeonggi-do 446-701,
Republic of Korea*

inosato@khu.ac.kr

T. Magara

*School of Space Research, Kyung Hee University, Yongin, Gyeonggi-do 446-701,
Republic of Korea*

V. S. Pandey

*Department of Physics, National Institute of Technology, Dwarka, Sector-9, Delhi-110077,
India*

D. Shiota

Solar-Terrestrial Environment Laboratory, Furo-Cho, Chikusa-ku Nagoya 464-8601, Japan

¹

K. Kusano

Solar-Terrestrial Environment Laboratory, Furo-Cho, Chikusa-ku Nagoya 464-8601, Japan

²

G. S. Choe, and K. S. Kim

*School of Space Research, Kyung Hee University, Yongin, Gyeonggi-do 446-701,
Republic of Korea*

¹ Computational Astrophysics Laboratory, RIKEN(Institute of Physics and Chemical Research), Wako, Saitama 351-0198, Japan

²Japan Agency for Marine-Earth Science and Technology (JAMSTEC),Yokohama, Kanagawa 236-0001, Japan

ABSTRACT

We develop a nonlinear force-free field (NLFFF) extrapolation code based on the magnetohydrodynamic (MHD) relaxation method. We extend the classical MHD relaxation method in two important ways. First, we introduce an algorithm initially proposed by Dedner et al. (2002) to effectively clean the numerical errors associated with $\nabla \cdot \mathbf{B}$. Second, the multi-grid type method is implemented in our NLFFF to perform direct analysis of the high-resolution magnetogram data. As a result of these two implementations, we successfully extrapolated the high resolution force-free field introduced by Low & Lou (1990) with better accuracy in a drastically shorter time. We also applied our extrapolation method to the MHD solution obtained from the flux-emergence simulation by Magara (2012). We found that NLFFF extrapolation may be less effective for reproducing areas higher than a half-domain, where some magnetic loops are found in a state of continuous upward expansion. However, an inverse S shaped structure consisting of the sheared and twisted loops formed in the lower region can be captured well through our NLFFF extrapolation method. We further discuss how well these sheared and twisted fields are reconstructed by estimating the magnetic topology and twist quantitatively.

1. Introduction

Solar active phenomena such as solar flares, coronal mass ejections (CMEs), and filament eruptions are widely attributed to the release of magnetic energy in the solar corona (Priest & Forbes 2002 and Shibata & Magara 2011). Many theoretical and numerical models have been proposed for understanding their dynamics and triggering mechanisms (The details are summarized in Linton & Moldwin 2009; Chen 2011; Shibata & Magara 2011.). However, a number of issues remain unanswered. For instance, we still do not have a proper view of the three-dimensional (3D) coronal magnetic field related to an active region. Earlier studies based on analytical or numerical models were categorized in terms of the 'loss of stability' or 'loss of equilibrium', however, there are also a few cases that strongly depend on the magnetic configurations because the coronal magnetic field deduced from observational images is very complicated, and one cannot extract its physical essence in term of the simplified analytical models. Therefore, it becomes important to construct the coronal magnetic field on the basis of a numerical model by using the observational data and to investigate the physical condition of the equilibrium state before the flare.

Unfortunately, the 3D coronal magnetic field cannot be directly observed even with the state-of-art solar physics satellite, whose observations can currently provide only the vector field on the photosphere. For these reasons, force-free extrapolation has been performed based on a vector field. The force-free field is expressed as follows;

$$\nabla \times \mathbf{B} = \alpha(r)\mathbf{B}, \quad (1)$$

or

$$\mathbf{B} \cdot \nabla \alpha(r) = 0, \quad (2)$$

and it has been widely accepted as an approximation of the coronal magnetic field because the value of the plasma β is very low ($10^{-1} \sim 10^{-2}$) in the solar corona. The force-free state is classified into three energy levels. One of them, called the potential field is the current free state *i.e.* $\alpha(r) = 0$, hence, this corresponds to the minimum energy state. The linear force-free field (LFFF) has a uniform distribution of $\alpha(r)$, and this energy level is higher than the potential field. However the observed α is generally a function of space on the photosphere.

Observations at various wavelengths often reveal a localized strong shear field close to the neutral line in the active regions before a flare (*e.g.*, Hagyard et al. (1984); Su et al. (2007)). From these observational images and results, we know that the potential and LFFF cannot adequately explain the coronal magnetic field before the flare; thus, the nonlinear force-free field (NLFFF) has been considered to model the active region's magnetic field. Because the force-free equation is essentially nonlinear, it is not straightforward to solve it for the coronal magnetic field. The solution is obtained only numerically through an iteration process for a fixed vector field on the bottom boundary, whereas the potential field and LFFF are calculated easily from the normal component of the magnetic field on the solar surface (Sakurai 1989). Various methods of obtaining NLFFF solutions have been proposed and developed. For the sake of brevity, we do not review them thoroughly here; interested readers are urged to see the comprehensive reviews on this topic by Schrijver et al. (2006), Metcalf et al. (2008) or Wiegelmann & Sakurai (2012).

Representative methods for extrapolating the force-free coronal magnetic field include time-evolutionary methods as well as iterative methods (*e.g.*, the boundary integral method of Yan & Sakurai 1997; Yan & Sakurai 2000 and the Grad-Rubin methods of Sakurai 1981; Amari et al. 1997; WHEATLAND 2004; Amari et al. 2006), which iterate an equation to find a solution(1). McClymont & Mikic (1994) and Mikic & McClymont (1994) developed the magnetohydrodynamic (MHD) relaxation method, which directly solves the MHD equations under the zero β approximation (Mikic et al. 1988). These equations include the resistivity which allows the field lines to change their topology rapidly toward a force-free state. The calculation begins with the construction of a potential field from the normal component

of the magnetic field on the photosphere and a force-free state is obtained by controlling the transverse electric field and keeping the magnetic flux B_z according to an induction equation toward the normal component of the current density deduced from the vector field. Jiang et al. (2011) and Jiang & Feng (2012) recently developed a force-free extrapolation code based on the MHD relaxation method that includes the gas pressure, viscous and resistive terms. That code is implemented into the space-time conservation-element and solution-element method constructed using full MHD system and a modern high-performance numerical method (Feng et al. 2007; Feng et al. 2010).

Roumeliotis 1996 developed a force-free extrapolation code that included an induction equation with a hypothetical velocity against the Lorentz force, which is a simplification from McClymont & Mikic (1994) and Mikic & McClymont (1994). This formula was originally introduced by Yang et al. (1986) to obtain a magneto-frictional method. In addition, this calculation is classified into two phases, stress and relaxation after a potential field is constructed as an initial state from the normal component of the magnetic field on the photosphere. In the stress phase a Lorentz force is injected from the bottom boundary so that the transverse components of the vector potential approach the observed transverse field. In the relaxation phase, the upper coronal field relaxes toward a force-free state under the fixed bottom boundary. Because of these two combined effects in this method, it is called stress and relaxation method. Some authors have already implemented this method into their own code (Valori et al. 2005; Jiang et al. 2011). The resistivity included in the induction equation permits the magnetic reconnection to accelerate the process of the force-free state; thus it plays the same role as in McClymont & Mikic (1994) and Mikic & McClymont (1994). Valori et al. (2005) introduced the magnetic induction field vector to replace the vector potential. This make it easier to implement the boundary condition than in the original stress and relaxation method of Roumeliotis (1996). They applied their extrapolation method to the twisted loops obtained from Török & Kliem (2003) and found that the NLFFF performs reasonably well for reconstructing of the twisted loops in the localized area close to the neutral line. The improved code of the Valori et al. (2007) and Valori et al. (2010) is applied to the ideal force-free field introduced by Low & Lou (1990) and also to a more complex situation by Titov & Démoulin (1999). van Ballegooijen (2004) inserts a twisted magnetic flux tube into a potential field and the magnetofriction (van Ballegooijen et al. 2000) drives as system toward a force-free state without the transverse component on the photosphere; its magnetic configuration is then compared with observational images. Another method is an optimization method originally proposed and developed by Wheatland et al. (2000) and an improved version of it presented by Wiegmann (2004), which minimizes a function consisting of divergence-free and force-free fields. Although the basic equation in the optimization method also includes a higher-order differential equation, which is difficult to solve

even numerically, highly accurate reconstruction is recorded in some papers (*e.g.*, Schrijver et al. 2006)

Recently the Solar Optical Telescope(SOT) on board *Hinode* (Kosugi et al. 2007 and Tsuneta et al. 2008) can provide images of the vector field with a high spatial resolution (more than 1K pixels). Moreover, the Helioseismic and Magnetic Imager (HMI) on board the *Solar Dynamics Observatory (SDO)* can provide vector field data with a high temporal resolution (every 12s), which enables analysis of the NLFFF in unprecedented temporal resolution. Thus it would be interesting to see the performance of the NLFFF with these high-resolution data.

The purpose of this study is to develop an extrapolation code for the NLFFF that accelerates the calculation time even when these high-resolution data are used. We extended the original MHD relaxation method of McClymont & Mikic (1994) and Mikic & McClymont (1994) in two important ways. First, we implemented an algorithm to prevent the deviation from $\nabla \cdot \mathbf{B} = 0$ introduced by Dedner et al. (2002), in which the time dependent term corresponding to ϕ (see equation 6) is used to remove the numerical error of $\nabla \cdot \mathbf{B}$. Second, we implemented a multi-grid-type method (Brandt 1977) to more rapidly propagate information on the boundary condition at a larger scale inside the domain than in the smaller component, which accelerates the speed towards a force-free state. The accuracy and reliability are investigated by using the ideal force-free solution introduced by Low & Lou (1990). We further apply our extrapolation code to the MHD solution obtained from the flux emergence simulation by Magara (2012) to investigate the reliability of the NLFFF extrapolation in a real physical situation.

This paper is constructed as follows. The extrapolation and numerical methods are described in Section 2. The result of the reconstruction using the Low & Lou solution is presented in Section 3 and whereas the MHD solution from Magara (2012) is shown in Section 4. Finally, some important discussions and conclusions are summarized in Section 5.

2. Numerical Method

We developed an NLFFF extrapolation code based on MHD relaxation by implementing the multi-grid-type procedure and an algorithm for cleaning the errors related to $\nabla \cdot \mathbf{B}$. We demonstrated the performance of this method in our previous studies, *e.g.*, Inoue et al. (2011), Inoue et al. (2012a), Inoue et al. (2012b) and Inoue et al. (2013). Nevertheless, several issues were not covered extensively in the previous works and require more detailed

explanations.

This method is formulated using the zero-beta MHD equations where the gas pressure and gravity are neglected (Mikic et al. 1988) to achieve a force-free state. In this study, we numerically solve the following equations

$$\frac{\partial \mathbf{v}}{\partial t} = -(\mathbf{v} \cdot \nabla) \mathbf{v} + \frac{1}{\rho} \mathbf{J} \times \mathbf{B} + \nu \nabla^2 \mathbf{v}. \quad (3)$$

$$\frac{\partial \mathbf{B}}{\partial t} = \nabla \times (\mathbf{v} \times \mathbf{B} - \eta \mathbf{J}) - \nabla \phi, \quad (4)$$

$$\mathbf{J} = \nabla \times \mathbf{B}. \quad (5)$$

$$\frac{\partial \phi}{\partial t} + c_h^2 \nabla \cdot \mathbf{B} = -\frac{c_h^2}{c_p^2} \phi, \quad (6)$$

where \mathbf{B} is the magnetic flux density, \mathbf{v} is the velocity, \mathbf{J} is the electric current density, ρ is the pseudo density, and ϕ is the convenient potential. The pseudo density is assumed to be proportional to $|\mathbf{B}|$ in order to ease the relaxation by equalizing the Alfvén speed in space. The last equation (6) introduced by Dedner et al. (2002) plays a crucial role in avoiding deviation from $\nabla \cdot \mathbf{B} = 0$. From equations (4) and (6), we can obtain the following equation:

$$\frac{\partial^2 (\nabla \cdot \mathbf{B})}{\partial t^2} + \frac{c_h^2}{c_p^2} \frac{\partial (\nabla \cdot \mathbf{B})}{\partial t} = c_h^2 \nabla^2 (\nabla \cdot \mathbf{B}), \quad (7)$$

which illustrates the propagating and diffusing nature of the numerical errors related to $\nabla \cdot \mathbf{B}$, where c_h and c_p correspond to the advection and diffusion coefficients, respectively. The main advantages of this method are that (I) it can be very easily implemented in our numerical code without the need for many improvements and (II) it accelerates the process of removing errors and does not take as much time as that required to remove errors by solving the Poisson equation (see Tóth 2000 or Tanaka 1995).

The length, magnetic field, velocity, time and electric current density are normalized by L_0 , B_0 , $V_A \equiv B_0/(\mu_0 \rho_0)^{1/2}$, $\tau_A \equiv L_0/V_A$, and $J_0 = B_0/\mu_0 L_0$, respectively. The non-dimensional viscosity ν is set to a constant, (1.0×10^{-3}), and the non-dimensional resistivity η is given by the functional

$$\eta = \eta_0 + \eta_1 \frac{|\mathbf{J} \times \mathbf{B}| |\mathbf{v}|^2}{|\mathbf{B}|^2}, \quad (8)$$

where, η_0 depends on each case, as shown in table 1, and η_1 is fixed at 1.0×10^{-3} in non-dimensional units. The second term is introduced to accelerate the relaxation to the force-free state particularly in the weak field region. The parameters c_p^2 are fixed at constants 0.1, whereas c_h^2 varies according to table 1.

The velocity field is adjusted in such a way that it does not correspond to a large value; otherwise, it would affect the Courant-Friedrichs-Lewy condition. We define $v^* = |\mathbf{v}|/|\mathbf{v}_A|$ and if the value of v^* becomes larger than the value of v_{max} as given in table 1, the velocity is modified as follows:

$$\mathbf{v} \Rightarrow \frac{v_{max}}{v^*} \mathbf{v}. \quad (9)$$

Two different types of boundary conditions are applied in this study to extrapolate the 3D coronal magnetic field. The first is that all six boundaries are set to the exact solutions obtained from Low & Lou. We denote this boundary condition as EX. In the second, only the bottom boundary is set to the exact solution from Low & Lou or Magara (2012) and the other boundaries are assumed to act like rigid walls; *i.e.*, the normal component of the magnetic field is fixed at the original solutions, and the tangential component is determined by the induction equation as described in equation (4). We denote this boundary condition as RW, which is less information than it in EX. In all cases, the velocity field (\mathbf{v}) is set to zero on all the boundaries. A Neumann-type boundary condition ($\partial_n \phi = 0$) is applied for the potential ϕ at all the boundaries, where ∂_n represents the derivative for the normal direction on the surface. The initial condition is given by a potential field calculated from the normal component on all the boundaries for all cases.

In the ideal force-free cases (the Low & Lou solution), we apply the exact solutions directly on each boundary surface. On the other hand, in the MHD solution obtained from Magara (2012), the handling of the bottom boundaries differs from that in the ideal force-free case except for the normal component. In this case, we introduce a procedure analogous to the stress and relaxation method. The transverse component \mathbf{B}_{BC} is defined as a linear combination of \mathbf{B}_{obs} and \mathbf{B}_{pot} on the bottom surface as follows:

$$\mathbf{B}_{BC} = \gamma \mathbf{B}_{obs} + (1 - \gamma) \mathbf{B}_{pot}, \quad (10)$$

where \mathbf{B}_{obs} and \mathbf{B}_{pot} are the transverse components of the observational (MHD solution in this study) and the potential field, respectively. γ is a coefficient ranging from range of 0 to 1. When $R = \int |\mathbf{J} \times \mathbf{B}|^2 dV$, which is introduced as an indication for the force-free state, drops below a critical value denoted by R_{min} during an iteration, then γ grows according to $\gamma = \gamma + d\gamma$, where $d\gamma$ is also given as a parameter. γ becomes equal to 1; then \mathbf{B}_{BC} can be completely consistent with the observational data.

As for the numerical method, the spatial derivative is approximated by the second-order finite difference and a time integration is conducted, using the Runge-Kutta-Gill method to fourth-order accuracy. Furthermore, we adapt the multi-grid-type method to accelerate the procedure for achieving a force-free state. This method contains the several distinct numerical grids with different resolutions; the first calculation starts using the coarsest one to obtain a force-free field, and then we use this as an initial condition for the second high-resolution grid. Consequently by repeating these procedures, the high-resolution force-free state can be obtained in a short time.

The simulation domain in the ideal force-free case is set to $(0, 0, 0) < (x, y, z) < (2, 2, 2)$ defined as non-dimensional values, and this is divided into 64^3 grids, 128^3 grids, 256^3 grids, or 512^3 grids, case3M1, case3M2, case1M1 and case1M2 shown in table 1 are applied for the multi-grid-type method, whereas direct calculation is applied for case0-case5, without it. On the other hand, for the MHD solution, the entire numerical domain is set to $(0, 0, 0) < (x, y, z) < (43.2, 43.2, 32.4)(\text{Mm}^3)$ following Magara (2012), and extracted from the original data; then the total grid number is assigned as $80 \times 80 \times 60$. All the parameters in each case are given in table 1. All of the physical values are normalized using $L_0 = 43.2(\text{Mm})$ and $B_0 = 262(\text{G})$ (see Magara & Longcope 2003 for details); consequently, the numerical domain is set to $(0, 0, 0) < (x, y, z) < (1, 1, 0.75)$ in non-dimensional space.

3. Result of the NLFFF Extrapolation of Low & Lou Solution

3.1. Role in the Cleaning of the Numerical Error Related to $\nabla \cdot \mathbf{B}$

We first check the accuracy of the numerical code for the ideal force-free solution introduced by Low & Lou (1990). A 3D view of this solution is shown in Figure 1 (a). The lines and background color indicate the magnetic field lines and distribution of the normal component of the magnetic field, respectively. Figure 1(b) shows the potential field extrapolated from the normal component of the magnetic field on all the boundaries, which is used as an initial condition in the NLFFF calculation. We calculated the three cases denoted as case i where $i = 0-2$. Case0 corresponds to the boundary condition EX, where we also do not use equation(6). Case1 and case2 correspond to the boundary conditions Ex and RW, respectively. More detailed informations on case1 and case2 are given in table 1.

Figures 2 (a) and (b) show iteration profiles of $R = \int |\mathbf{J} \times \mathbf{B}|^2 dV$ and $D = \int |\nabla \cdot \mathbf{B}|^2 dV$ for different cases. We clearly found that case1 and case2 tends toward a force-free state, because the R and D profiles decrease with each iteration. Iteration was stopped when R reached a minimum value. Case0 shows a much different profile from those of case1 and

case2. This result indicates that an iteration profile approaching a force-free state is very sensitive to numerical errors in the deviation from $\nabla \cdot \mathbf{B} = 0$. The difference between case1 and case2 is determined by the differences in the lateral and top boundary conditions between them. Even though incomplete lateral and top boundaries in RW are given in case2, the values of R and D are found to be equal order of magnitude of that in case1. However, case2 takes about twice as long as case1 to search for the force-free solution.

3.2. Topology Analysis of the 3D Magnetic Field Lines

The three-dimensional NLFFF structures for case1 and case2 are shown in Figures 3(a) and (b), respectively. The Color contours represent a connectivity error that is defined as

$$\Delta = |\Delta_{Exact} - \Delta_{NLFFF}|. \quad (11)$$

Δ_{Exact} (Δ_{NLFFF}) is the distance from one magnetic field line footpoint to another measured on the bottom surface in the exact(NLFFF) solution. The NLFFF solutions in case1 and case2 seem to have almost the same configuration as that of the exact Low & Lou solution shown in Figure 1(a). The connectivity errors between these cases also have the same distributions, a random distribution in the entire domain.

We investigate the magnetic topology to clarify the cause of the connectivity error. We used the photospheric cross-section of the quasi-separatrix layers (QSLs) introduced by Demoulin et al. (1996). We calculated the following quantity at each pixel on the vector field maps:

$$N(x, y) = \sqrt{\sum_{i=1,2} \left[\left(\frac{\partial X_i}{\partial x} \right)^2 + \left(\frac{\partial X_i}{\partial y} \right)^2 \right]}, \quad (12)$$

where (X_1, X_2) is the relative distance corresponding to $(x' - x'', y' - y'')$. (x', y') and (x'', y'') are the positions of the end points of the field lines whose starting points are two adjacent grid points located at (x'_0, y'_0) and (x''_0, y''_0) on the photospheric surface. This means that the locations of the end points of these field lines, which are traced from these start points across a large $N(x,y)$ value, may differ greatly.

Figures 3(c) and (d) show the connectivity error in white contours whose magnitude corresponding to 0.05 over the distribution $\log(N)$ mapped on the bottom surface. We clearly see that the connectivity errors are almost on the enhancement layers at considerable distance from a polarity inversion line. From this analysis, we found that, remarkably, the error in the NLFFF appears in particular regions where the magnetic topology is changing dramatically.

We show these particular regions in detail. Figures 3(e) and (f) show the connectivity errors in the same format as Figures 3(c) and (d) over a map of the open-closed field lines in case1 and case3, respectively. Closed means that both footpoints of each field line are anchored in the bottom surface; for the open field, one footpoint goes through the side or top boundaries. These results clearly show that the connectivity errors appear along the boundaries between open and closed field lines. On the other hand, the values obtained from this study are ~ 0.5 , but most of regions are occupied by values less than 0.25, which is much smaller than the entire length of the numerical domain. Consequently, this is not due to a change in the topology from open to closed lines or vice versa; rather, each outer loop of the open or closed field lines deviates slightly from the reference field. Furthermore, Figure 3(f) shows a plot in the same format with a higher resolution than that of Figure 3(e), which can reduce the error distribution.

3.3. Quantitative Comparison of Low & Lou solution and NLFFF

We further performed a detailed quantitative analysis as introduced by Schrijver et al. (2006). When \mathbf{B} and \mathbf{b} represent the semi-analytical Low & Lou solution and the extrapolated solution, respectively, the accuracy of the NLFFF is estimated by the following sequential relations;

$$C_{vec} \equiv \frac{\sum_i \mathbf{B}_i \cdot \mathbf{b}_i}{(\sum_i |\mathbf{B}_i|^2 \sum_i |\mathbf{b}_i|^2)^{1/2}}, \quad (13)$$

$$C_{cs} \equiv \frac{1}{N} \sum_i \frac{\mathbf{B}_i \cdot \mathbf{b}_i}{|\mathbf{B}_i| |\mathbf{b}_i|}, \quad (14)$$

$$1 - E_N \equiv 1 - \frac{\sum_i |\mathbf{b}_i - \mathbf{B}_i|}{\sum_i |\mathbf{B}_i|}, \quad (15)$$

$$1 - E_M \equiv 1 - \frac{1}{N} \sum_i \frac{|\mathbf{b}_i - \mathbf{B}_i|}{|\mathbf{B}_i|}, \quad (16)$$

$$\epsilon \equiv \frac{\sum_i |\mathbf{b}_i|^2}{\sum_i |\mathbf{B}_i|^2}, \quad (17)$$

where C_{vec} is the vector correlation, C_{cs} is the Cauchy-Schwarz inequality, E_M is the mean vector error, E_N is the normalized vector error, ϵ is the energy ratio, and N is the number of vectors in the field. These results are summarized in table.2. Figure 4(a) shows the iteration profiles of $1 - E_m$ for case1 and case2. The final values reach 0.95 in both cases. We

clearly see that both case1 and case2 can reconstruct the original Low & Lou solution with good accuracy and no significant difference is found between them even though case2 takes a longer calculation time than case1.

Finally, we performed another quantitative analysis by evaluating the force-free α in both footpoints of each field line. Because the value of the force-free α should be constant along the field line (cf., equation (2)) their values at the both footpoints of each field line should be equal in order to satisfy the force-free condition. The force-free α in both footpoints for case1 and case2, measured on the surface above first grid above the bottom one, are mapped in Figures 4(b) and (c), respectively. The horizontal and vertical axes represent the values of the force-free α at each footpoint where the diagonal green line corresponds to $y = x$. If an extrapolated field completely satisfies the force-free state, the force-free α will be distributed along this line. Because most points in case1 and case2 are along the green line, this result clearly shows that these cases almost satisfy the force-free state well.

3.4. Multi-Grid Strategy

3.4.1. Procedure of the Multi-grid type method

We present a procedure for a multi-grid-type method, which is needed to accelerate the calculation time for high-resolution magnetogram data obtained from *e.g.*, SOT/*Hinode*. Some algorithms have already implemented it, and an accelerated calculation speed was reported (*e.g.*, Metcalf et al. 2008 and Jiang & Feng 2012). First, we extrapolate an NLFFF with the coarsest grid n_{min}^3 , to rapidly propagate large-scale information from a boundary into an interior domain. When the value of R ($\int |\mathbf{J} \times \mathbf{B}|^2 dV$) reaches a minimum the grid number is changed to $(2n_{min})^3$ by using a linear interpolation; the exact boundary conditions are maintained, and its location and other parameters are fixed as those in the previous calculation except that η_0 set to zero. This process is repeated until a force-free field is achieved under given grid points with the highest resolution; therefore, this method is not a full multi-grid method. The detailed information is given in the Table.1.

3.4.2. Accuracy and Calculation Time in Run1

We performed our calculations using two different patterns, *i.e.*, run1 and run2, using a multi-grid-type method whose final results are obtained in three steps. First, we examined the performance related to run1 with an initially assignment of the coarsest grid number 128^3 grid points denoted as case3. After attaining a force-free state with this number of grid

points, a higher resolution of (256^3) was obtained by using the force-free field realized in the previous step as an initial condition, which is referred to case3M1. In the same way, the highest resolution of (512^3) was achieved in case3M2. For comparison with case3M1, we also calculated case4, in which 256^3 grid points are assigned, but without an implementation of the multi-grid-type method.

Figures 5(a) and (b) show the results related to iteration profiles of $R = \int |\mathbf{J} \times \mathbf{B}|^2 dV$ and $D = \int |\nabla \cdot \mathbf{B}|^2 dV$ corresponding to run1. The coarsest grid level 128^3 gradually decreases by 1.0×10^{-7} at about 2.0×10^4 iterations; the calculation takes 12h^1 in real time and $1 - E_m$ reaches about 0.98, as shown in Table.2. Although R and D suddenly increase as the grid number changes from 128^3 to 256^3 , they immediately decrease by about 1.0×10^{-7} again. This sudden increment in R and D due to the change in the grid is clearly the result of a numerical error arising from an interpolation. However, this error rapidly decreases within 10^3 iterations, as this scale is small compared to the previous grid, so the diffusion may be effective in decreasing the numerical error associated with a higher mode. The green line corresponding to 256^3 grids can reach 1.0×10^{-7} at about 3.0×10^4 iterations, which is marked by the green circle; the total calculation time takes about 45 h in real time. On the other hand, in case4, which is also assigned to the 256^3 grids but without the multi-grid-type method, the value of R marked after a total calculation time of 100 h, by a black circle, is found to be one order larger than that for case3M1. The multi-grid-type method significantly reduces the calculation time. Hence, we clearly see that it is an effective method for analyzing high resolution data. The final state, plotted by the purple lines, can achieve a high-resolution force-free field given by 512^3 grids.

Figures 5(c) shows a distribution map of the force-free α for case3M1 at the green solid circle in Figure 5(a); the map is in the same format as Figures 4(b) or (c). We see that many red points appear along the green lines although a slight deviation appears in the range of $0 < \alpha < 2.0$. However, the overall pattern of the extrapolated field satisfies a state close to the force-free state. On the other hand, Figure 5(d) shows the results for the case4, marked by the dotted black circle in Figure 5(a), where the calculation time is the same as that for 3.0×10^4 iterations at the end of the calculation in case3M1. As expected, many points deviate from the force-free state. Thus, an implementation of the multi-grid-type method yields a force-free state in a dramatically short time.

¹Numerical code was parallelized by Message Passing Interface (MPI) and the calculation speed was measured by using a 3.06GHz Xeon X5500 eight-core processor implemented in DELL T7500.

3.4.3. Accuracy and Calculation Time in Run2

The procedure for run2 is basically the same as that of run1 except for the assigned grid numbers. In run2 64^3 grids points are initially assigned, corresponding to the coarsest grid and initial condition in case1. Eventually, following the same procedure in run1, we obtain a force-free state with 128^3 and 256^3 grid points, which are called case1M1 and case1M2, respectively.

Figures 6(a) and (b) show the results on the R and D profiles, respectively, for each case (case1, case1M1, and case1M2). The black line corresponds to case4, which is the same as in run1. The green and black solid circles represent 2.0×10^4 iterations, corresponding to the end of the calculation with 256^3 grid points, for case1M2 and case4, respectively. The total calculation times were approximately 30 h and 67h, respectively. Further, the black dotted circle represents 8625 iterations for case4, corresponding to the same calculation time as that required for 2.0×10^4 iterations of the multi-grid-type case. Although the R and D profiles in multi-grid cases reach to values of less than 1.0×10^{-7} , as with the previous multi-grid-type case, run1, the quantitative value $1 - E_m$ shown in table 2 does not increase from its initial value of 0.95 (obtained from the initial coarsest grid) with increasing grid numbers. We further checked the distribution map of the force-free α .

Figures 6(c) and (d) show a distribution map of the force-free α for case1M2 and case4, marked by the solid green and dotted black circles, respectively, in Figure 6(a); the format is the same as in Figures 5(c) or (d). Case1M2 in the region $\alpha < 0$ is found to yield a better reconstruction in a short time than case4. However, for $0 < \alpha < 3.0$, this case, as well as case3M1, seems to deviate slightly from the force-free state. In comparison, Figure 4(b), which shows a distribution map of the force-free α in the initial state, shows a better force-free state than case1M2 even for $\alpha > 0$. Hence, this error is clearly derived from an interpolation through a change in the grid that critically affects the value of $1 - E_m$, as reported by Jiang & Feng (2012).

3.5. 2D Distribution of the Force-Free α

Figure 7(a) plots contours of the force-free α to clarify why the reconstructed field in the region of weak force-free α ($0 < |\alpha| < 3.0$) deviated from the force-free state when the multi-grid-type method is used, as such as shown in Figures 5 and 6. The red, green, and blue contours indicate strengths of the force-free α corresponding to 2.0, -2.0 , and -4.0 , respectively. From Figure 7(a), a region of strong force-free α appears in the central region, where the extrapolated field satisfies the force-free state well, as shown in the previous

results. On the other hand regions of weak negative and positive force-free α , R1 and R2 lie at considerable distances from the central region in the numerical domain where the force-free α is distributed in a range of $2.0 < \alpha < 4.0$ and $-2.0 < \alpha < 0$, respectively. Figure 7(b) also shows the magnetic field lines, most of which in R1 and R2 are rooted in a region near the boundaries of the domain; *i.e.*, the numerical errors remarkably appear near the boundaries through an interpolation accompanying a change in the grid number. However, as in Figure 6, the extrapolated field in the strong force-free α regions exhibits a better force-free state even when the multi-grid process is used. Thus, the core region in particular can be reconstructed with good accuracy in a dramatically short time by using it.

4. NLFFF Extrapolation in a Flux Emergence Region Produced by the MHD Simulation

We found that our NLFFF extrapolation method performed remarkably well in reproducing an ideal force-free state. Next, we applied it to a flux-emergence region obtained from an MHD simulation (Magara 2012). The idea was to check its performance for a region that is quite close to the real corona. The simulation results of the Magara (2012) provided a hypothetical state of the solar corona affected by the pressure, gravity field, and non-equilibrium state that differs greatly from the ideal force-free field introduced by Low & Lou. In this study, we focus on how well the sheared and twisted field lines in the lower corona are reconstructed by our NLFFF method; most of the free energy is accumulated in these lines, and they are treated as the most important parts for solar active phenomena such as solar flares and CMEs. In the following section, we quantitatively compare the differences in the 3D configurations yielded by the MHD solution and NLFFF extrapolation and finally estimate the degree of twist in them.

4.1. Overview of the Active Region from the MHD Simulation

Magara (2012) surveyed the dynamics of flux emergence with respect to a wide range of parameters set at the initial time of the twisted magnetic flux tube. In this study, we select one snapshot at the last moment of the MT case (see Table 1 in their paper), in which a flux tube embedded in the convection zone has emerged into the solar corona and formed coronal magnetic loops. First, we introduce the basic components of the magnetic field obtained from the MHD simulation, which is used as the boundary condition in our NLFFF extrapolation method.

Figure 8(a) shows a height profile of the integrated plasma β defined as $\langle \beta(z) \rangle = 2 \langle P(z) \rangle / \langle B^2(z) \rangle$, where $\langle P(z) \rangle$ and $\langle B^2(z) \rangle$ represent the average plasma and magnetic pressure, respectively, in a horizontal plane; $\langle P(z) \rangle = \int_{S_{xy}} P(x, y, z) dx dy$ and $\langle B^2(z) \rangle = \int_{S_{xy}} B^2(x, y, z) dx dy$. Near the bottom surface, a high- β ($1 \leq \langle \beta \rangle \leq 100$) regime is formed, which is suddenly converted into a low- β regime ($\ll 1$) around an intermediate height and finally again reaches a value similar to that at the bottom boundary as the height increases. We select the boundary condition at $\langle \beta \rangle = 0.06$ which corresponds to case5 (marked by solid circles). The distribution of the normal component of the magnetic field in case5 is shown in Figure 8(b). It is formed by the emerging flux tube at 2700(km) above photosphere in the MHD simulation. The value of the magnetic field is normalized by its maximum value at this height. Hereafter, this height is regarded as the bottom surface.

Figure 8(c) shows height profiles of the integrated force-free α ($\langle \alpha \rangle$) and the non-force-free component ($\langle \alpha' \rangle$), denoted as

$$\langle \alpha \rangle = \int_{S_{xy}} \frac{|\mathbf{J} \cdot \mathbf{B}|}{|\mathbf{B}|^2} dx dy, \quad (18)$$

$$\langle \alpha' \rangle = \int_{S_{xy}} \frac{|\mathbf{J} \times \mathbf{B}|}{|\mathbf{B}|^2} dx dy. \quad (19)$$

The value of $\langle \alpha \rangle$ is larger than that of $\langle \alpha' \rangle$ in those regimes where the condition of low $\langle \beta \rangle$ is satisfied well. The solid circle indicates the result for the case5, where $\langle \alpha \rangle$ is competing with $\langle \alpha' \rangle$.

However, this MHD solution does not satisfy the equilibrium state completely; therefore, we have to estimate the degree to which the Lorentz force is accumulated in the selected boundary condition, as shown in Figure 8(b). We estimate it using the following values:

$$\epsilon_{force} = \frac{(|\int_S B_x B_z| + |\int_S B_y B_z| + |\int_S ((B_x^2 + B_y^2) - B_z^2)|) dx dy}{\int_S (B_x^2 + B_y^2 + B_z^2) dx dy},$$

$$\epsilon_{torque} = \frac{(|\int_S x((B_x^2 + B_y^2) - B_z^2)| + |\int_S y((B_x^2 + B_y^2) - B_z^2)| + |\int_S y B_x B_z - x B_y B_z|) dx dy}{\int_S \sqrt{x^2 + y^2} (B_x^2 + B_y^2 + B_z^2) dx dy},$$

where S represents a surface on the bottom boundary, and ϵ_{force} and ϵ_{torque} correspond to the force balance and torque balance parameters, respectively. When $\epsilon_{force} \ll 1$ and $\epsilon_{torque} \ll 1$, the boundary surface approximately satisfies the force-free condition (Wiegelmann et al. 2006). As a result, in this case ($\epsilon_{force} = 0.275$ and $\epsilon_{torque} = 0.382$), they deviate from the

force-free state; nevertheless these values are close to the SP/*Hinode* data for Dec.12, 2006 according to Wiegmann et al. (2012).

Figure 8(d) shows profiles of the integrated velocity with respect to the y direction ($\int |\mathbf{v}(x, y, z)| dy$) with a map of the current density in the same format as ($\int |\mathbf{J}(x, y, z)| dy$). We clearly see that the color is strongly enhanced in the lower central area in which the core field is formed. The large velocity fields, plotted by the white contours, are concentrated on the area around the half-height of the entire box, marked by the red dashed line. Consequently, we infer that extrapolation of this region is difficult; however, one of our interests is to address how well the core field is reconstructed under this condition.

4.2. Result of the NLFFF

4.2.1. 1D Profiles from the NLFFF and MHD Solutions

First, we show the one-dimensional result from the NLFFF and compare them with the MHD solution. Figure 9(a) shows iteration profiles of the total Lorentz force R (solid line) and magnetic energy E (dashed line) corresponding to case5. γ as defined in the equation (10) is equal to 1, and the other parameters used in this NLFFF calculation are shown in Table 1 (see case5). The NLFFF is selected at 1.0×10^4 iterations, at approximately which R and E begin to saturate.

Figure 9(b) shows the height profiles of $\langle \alpha \rangle$ in the MHD solution (dashed line) and $\langle \alpha_{nlfff} \rangle$ in NLFFF (solid line) for case5. The values of $\langle \alpha_{nlfff} \rangle$ and its pattern deviates slightly from those of $\langle \alpha \rangle$ corresponding to those regimes where the value of $\langle \alpha \rangle$ is dominant over $\langle \alpha' \rangle$, as shown in Figure 8(b). On the other hand, these values and profiles of $\langle \alpha_{nlfff} \rangle$ are found to deviate greatly from those of $\langle \alpha \rangle$ in the upper area, above the half-height of the entire domain.

4.2.2. 3D Magnetic Structures and Topologies in the NLFFF and MHD Simulations

Next, we show a 3D view of the MHD simulation and NLFFF and present a detailed comparison in terms of the magnetic topology. Figure 10(a) shows a top view of the selected field lines obtained from the MHD solutions for case5. These are traced from the surface, which is 2700(km) above the photosphere, as shown in Figure 8(a). Figure 10(b) also shows the selected 3D field lines in the NLFFF, which are also extrapolated from the same surface as those described above. From these results, we infer that although they are not exactly

the same, the NLFFF seems to reproduce an inverse S shaped structure lying above the polarity inversion line and is qualitatively similar to the MHD solution. It is important to capture these S or inverse S shaped structures because they are considered to be precursors for huge flares (Canfield et al. 1999) observed in solar active regions. We further investigate the magnetic topology in more detail to clarify the differences in between the NLFFF and MHD solutions.

Figures 10(c) and (d) show the distribution of the field line length mapped on the bottom surface for the MHD solution and the NLFFF, respectively. One footpoint of the field lines rooted in the white areas is not at the bottom surface; that is, their other footpoints is rooted in the lateral boundary surfaces, whereas the other field lines traced from colored areas are closed. Therefore, the boundaries between the colored and white areas represent the separatrix separating the closed and open field lines, in which the QSL values are enhanced. The inverse S shaped structure can be formed by the NLFFF as well as by the MHD solution, and this structure is better captured in the NLFFF except in the regions marked by the dashed circle in which the closed loops are anchored.

To provide more clarification, we also show the field line structure within the dashed circle in Figure 10(d) in more detail. Figures 11(a) and (b) show the field lines (red) in the MHD and NLFFF, respectively, traced from the area marked by the dashed circle in Figure 10(d). The field line profiles in MHD and NLFFF are remarkably different. One footpoint of the field line in the MHD solution touches the lateral surface: i.e., the line crosses the boundary surface, whereas both footpoints in the NLFFF touch the bottom surface. Figures 11(c) and (d) show the distribution of the height of one footpoint of the field line measured from bottom surface in the MHD and NLFFF. All of the field lines are traced from the bottom surface, and most of their footpoints appear in the lower areas plotted in red. On the other hand, we see strong enhancement areas, which are marked by dashed circles, in the MHD solution, whereas these regions are not seen in the NLFFF. These enhanced areas indicate that the height of one footpoint of the field lines is above the half-height of the numerical domain; therefore, it might be difficult for the NLFFF to capture these field lines in this case.

4.2.3. *Magnetic Twist in the NLFFF and MHD Simulations*

Finally we compare the magnetic twist obtained using the NLFFF with that in the MHD solution. This value represents the degree of twist of a magnetic field line as determined by the measurement of the magnetic helicity generated due to the current parallel to a field line (Berger & Field 1984; Berger & Prior 2006; Török et al. 2010; Inoue et al. 2011; Inoue et al.

2012b; Inoue et al. 2013). Because a large amount of magnetic twist can lead to an unstable condition (Kruskal & Kulsrud 1958; Hood & Priest 1979; Török et al. 2004; Török & Kliem 2005; Fan 2005; Inoue & Kusano 2006; Birn et al. 2006), an estimation of the magnetic twist is important for analyzing the stability of the solar coronal magnetic field. We are interested in addressing the extent to which the magnetic twist can be reconstructed. The magnetic twist is defined as,

$$T_n = \frac{1}{4\pi} \int \alpha dl, \quad (20)$$

where the line integral $\int dl$ is taken along a magnetic field line, and the force-free α is calculated from $\alpha = \mathbf{J} \cdot \mathbf{B}/|\mathbf{B}|^2$.

Figure 12 shows the distributions of the magnetic twist in each field line from the MHD solution, where the NLFFF is also mapped on the surfaces at the same height. Positive and negative values indicate right-handed and left-handed twists, respectively, depending on the value of the magnetic helicity accumulated in an initial flux tube embedded in the subsurface. The black contours show the normal component of the magnetic field. We clearly see that the strongly twisted regions in the MHD solution are localized at positive and negative polarities, in which the strong twist values over one turn ($|T_n| > 1.0$) are found near the vicinity of the tip. In contrast, although the strongly twisted regions in the NLFFF are also localized in the same areas at the both polarities, their distributions and values are not the same as those of the MHD solution. The areas marked by the red circles are remarkably different in both cases; in the NLFFF, closed field lines exist in these areas, whereas that type of field line is not seen in the MHD solution. Although the reconstructed twisted lines in other areas tend to capture those in the MHD solution, their values are relatively weak in most regions near the tip at both polarities, whereas a high twist value, $|T_n| > 1.0$, is also observed in some areas. These results show that the shape of the sheared field lines is reconstructed well qualitatively; on the other hand, the value of the magnetic twist tends to be weaker than that of the reference field.

5. Summary & Discussion

In this study, we developed an NLFFF extrapolation code based on the MHD relaxation method and applied it to the ideal force-free field introduced by Low & Lou (1990). Our NLFFF extrapolation code generally produces the original ideal force-free state, even though incomplete lateral and top boundary conditions are imposed. Moreover, although errors related to the connectivity of the field lines clearly appeared along the separatrix layers (QSL), their topology is not changed dramatically. We further implemented the multi-grid-type method in our NLFFF extrapolation code, which increased calculation speed toward

a force-free state compared to the code without it. We see that the inner region of the numerical domain in particular can be reconstructed with high accuracy. Thus, our code can be used as a possible method for extrapolating the NLFFF in a shorter time using a high-resolution vector field obtained from SOT/*Hinode* or HMI/*SDO*.

Next, we also applied our extrapolation method to the MHD solutions obtained from Magara (2012), which are influenced by the gas pressure, gravity, and non-equilibrium state. In principle, it does not seem appropriate to apply the NLFFF to MHD solutions; nevertheless, in the interest of readers, we also checked the effectiveness of the NLFFF extrapolation for a more realistic situation of the solar corona. As a result, we found that the S-shaped sheared structure formed in the lower corona can be captured well by our NLFFF despite the difference in the value of the twist and the profile compared to the original MHD solutions. Thus, we conclude that our NLFFF extrapolation can work in the lower coronal region, in which a strong current is stored.

Our NLFFF extrapolation may be less effective for reproducing the upper region of the entire numerical domain. Note, however, that the numerical solutions of Magara (2012) describe an extreme situation compared to the real solar corona. For example, a pre-existing coronal field is not assumed in this MHD simulation, and in such a situation the magnetic loops filling the upper area can expand continuously in all directions, as pointed out by Magara (2004) and Magara (2011) (see Figure 8). Therefore, it might be difficult for the NLFFF to reconstruct this type of field line, as shown in our results (Figures 11 and 12). We believe that a consideration of the pre-existing coronal magnetic field may be important in suppressing the expanded loops during the process of flux emergence and achieving a steady state under which an S or inverse S-shaped field may be formed. We expect that our NLFFF extrapolation might be able to reproduce these regions with better accuracy than that in the results presented here. These results are derived from one of the results of Magara (2012), and our interests are in further addressing the extrapolation of the coronal magnetic field using boundary conditions formed by stronger or weaker twisted flux tubes, or with various plasma β values. However, these remain as future works.

On the other hand, a non-force-free extrapolation method has been developed recently by other authors (*e.g.*, Wiegmann & Neukirch 2006; Hu & Dasgupta 2008; Zhu et al. 2013; Gilchrist & Wheatland 2013). These methods are still being improved and are expected to be a solid tool for capturing the MHD solution more accurately in the near future.

From this study, we conclude that the extrapolated field can robustly reproduce an ideal force-free state, *e.g.*, the Low & Lou solution. In contrast for the MHD solutions obtained from the flux-emergence simulation, this method captures the sheared field, such as elbow-like structures lying in the lower corona, in which the strongest energy is accumulated.

Therefore, the extrapolated field may provide a better understanding of active phenomena in the solar corona. Because the SP/*Hinode* and HMI/*SDO* can observe the vector field with high spatial and temporal resolution, we will consider a comprehensive view of the flare dynamics and onset mechanism by using the 3D extrapolated magnetic field obtained from this data set in a future work.

We extend special thanks to Drs. T. Miyoshi, and K. Hayashi for many helpful discussions and anonymous referee for constructive comments. S. I. was supported by the International Scholarship of Kyung Hee University. G. S. C. was supported by the National Research Foundation of Korea (NRF-2010-0025403), and he thanks kyung Hee University for granting him a sabbatical in the 2012-2013 school year, during which his part of this research was performed. This research was supported by the BK21 plus program through the National Research Foundation (NRF) funded by the Ministry of Education of Korea, and by the Meteorological Administration of Korea through the National Meteorological Satellite Center. The computational work was carried out within the computational joint research program at the Solar-Terrestrial Environment Laboratory, Nagoya University. Part of computer simulation was performed on the Fujitsu PRIMERGY CX250 system of the Information Technology Center, Nagoya University. Part of computations, data analysis and visualization are performed using resource of the OneSpaceNet in the NICT Science Cloud.

REFERENCES

- Amari, T., Aly, J. J., Luciani, J. F., Boulmezaoud, T. Z., & Mikic, Z. 1997, *Sol. Phys.*, 174, 129
- Amari, T., Boulmezaoud, T. Z., & Aly, J. J. 2006, *A&A*, 446, 691
- Berger, M. A., & Field, G. B. 1984, *Journal of Fluid Mechanics*, 147, 133
- Berger, M. A., & Prior, C. 2006, *Journal of Physics A Mathematical General*, 39, 8321
- Birn, J., Forbes, T. G., & Hesse, M. 2006, *ApJ*, 645, 732
- Bobra, M. G., van Ballegooijen, A. A., & DeLuca, E. E. 2008, *ApJ*, 672, 1209
- Brandt, A. 1977, *Mathematics of Computation*, 31, 138
- Canfield, R. C., Hudson, H. S., & McKenzie, D. E. 1999, *Geophys. Res. Lett.*, 26, 627
- Chen, P. F. 2011, *Living Reviews in Solar Physics*, 8, 1

- Dedner, A., Kemm, F., Kröner, D., Munz, C.-D., Schnitzer, T., & Wesenberg, M. 2002, *Journal of Computational Physics*, 175, 645
- Demoulin, P., Henoux, J. C., Priest, E. R., & Mandrini, C. H. 1996, *A&A*, 308, 643
- Fan, Y. 2005, *ApJ*, 630, 543
- Feng, X., Zhou, Y., & Wu, S. T. 2007, *ApJ*, 655, 1110
- Feng, X., Yang, L., Xiang, C., et al. 2010, *ApJ*, 723, 300
- Gilchrist, S. A., & Wheatland, M. S. 2013, *Sol. Phys.*, 282, 283
- Hagyard, M. J., Teuber, D. , West, E. A., & Smith, J. B. 1984, *Sol. Phys.*, 91, 115
- Hu, Q., & Dasgupta, B. 2008, *Sol. Phys.*, 247, 87
- Inoue, S., & Kusano, K. 2006, *ApJ*, 645, 742
- Inoue, S., Kusano, K., Magara, T., Shiota, D., & Yamamoto, T. T. 2011, *ApJ*, 738, 161
- Inoue, S., Magara, T., Watari, S., & Choe, G. S. 2012, *ApJ*, 747, 65
- Inoue, S., Shiota, D., Yamamoto, T. T., et al. 2012, *ApJ*, 760, 17
- Inoue, S., Hayashi, K., Shiota, D., et al. 2013, *ApJ*, 770, 79
- Hood, A. W., & Priest, E. R. 1979, *Sol. Phys.*, 64, 303
- Jiang, C., Feng, X., Fan, Y., & Xiang, C. 2011, *ApJ*, 727, 101
- Jiang, C., & Feng, X. 2012, *ApJ*, 749, 135
- Kosugi, T., Matsuzaki, K., Sakao, T., et al. 2007, *Sol. Phys.*, 243, 3
- Kruskal, M. D., & Kulsrud, R. M. 1958, *Physics of Fluids*, 1, 265
- Linton, M. G., & Moldwin, M. B. 2009, *Journal of Geophysical Research (Space Physics)*, 114, 0
- Low, B. C., & Lou, Y. Q. 1990, *ApJ*, 352, 343
- Magara, T., & Longcope, D. W. 2003, *ApJ*, 586, 630
- Magara, T. 2004, *ApJ*, 605, 480
- Magara, T. 2011, *ApJ*, 731, 122

- Magara, T. 2012, ApJ, 748, 53
- McClymont, A. N., & Mikic, Z. 1994, ApJ, 422, 899
- Metcalf, T. R., De Rosa, M. L., Schrijver, C. J., et al. 2008, Sol. Phys., 247, 269
- Mikic, Z., Barnes, D. C., & Schnack, D. D. 1988, ApJ, 328, 830
- Mikic, Z., & McClymont, A. N. 1994, Solar Active Region Evolution: Comparing Models with Observations, 68, 225
- Priest, E. R., & Forbes, T. G. 2002, A&A Rev., 10, 313
- Roumeliotis, G. 1996, ApJ, 473, 1095
- Sakurai, T. 1981, Sol. Phys., 69, 343
- Sakurai, T. 1989, Space Sci. Rev., 51, 11
- Schrijver, C. J., et al. 2006, Sol. Phys., 235, 161
- Shibata, K., & Magara, T. 2011, Living Reviews in Solar Physics, 8, 6
- Su, Y., Golub, L., van Ballegoijen, A., et al. 2007, PASJ, 59, 785
- Tanaka, T. 1995, J. Geophys. Res., 100, 12057
- Titov, V. S., & Démoulin, P. 1999, A&A, 351, 707
- Török, T., & Kliem, B. 2003, A&A, 406, 1043
- Török, T., Kliem, B., & Titov, V. S. 2004, A&A, 413, L27
- Török, T., & Kliem, B. 2005, ApJ, 630, L97
- Török, T., Berger, M. A., & Kliem, B. 2010, A&A, 516, A49
- Tóth, G. 2000, Journal of Computational Physics, 161, 605
- Tsuneta, S., Ichimoto, K., Katsukawa, Y., et al. 2008, Sol. Phys., 249, 167
- Valori, G., Kliem, B., & Keppens, R. 2005, A&A, 433, 335
- Valori, G., Kliem, B., & Fuhrmann, M. 2007, Sol. Phys., 245, 263
- Valori, G., Kliem, B., Török, T., & Titov, V. S. 2010, A&A, 519, A44

- van Ballegoijen, A. A., Priest, E. R., & Mackay, D. H. 2000, *ApJ*, 539, 983
- van Ballegoijen, A. A. 2004, *ApJ*, 612, 519
- Wheatland, M. S., Sturrock, P. A., & Roumeliotis, G. 2000, *ApJ*, 540, 1150
- WHEATLAND, M. S. 2004, *Sol. Phys.*, 222, 247
- Wiegelmann, T. 2004, *Sol. Phys.*, 219, 87
- Wiegelmann, T., & Sakurai, T. 2012, *Living Reviews in Solar Physics*, 9, 5
- Wiegelmann, T., Inhester, B., & Sakurai, T. 2006, *Sol. Phys.*, 233, 215
- Wiegelmann, T., Thalmann, J. K., Inhester, B., et al. 2012, *Sol. Phys.*, 281, 37
- Wiegelmann, T., & Neukirch, T. 2006, *A&A*, 457, 1053
- Yan, Y., & Sakurai, T. 1997, *Sol. Phys.*, 174, 65
- Yan, Y., & Sakurai, T. 2000, *Sol. Phys.*, 195, 89
- Yang, W. H., Sturrock, P. A., & Antiochos, S. K. 1986, *ApJ*, 309, 38
- Zhu, X. S., Wang, H. N., Du, Z. L., & Fan, Y. L. 2013, *ApJ*, 768, 119

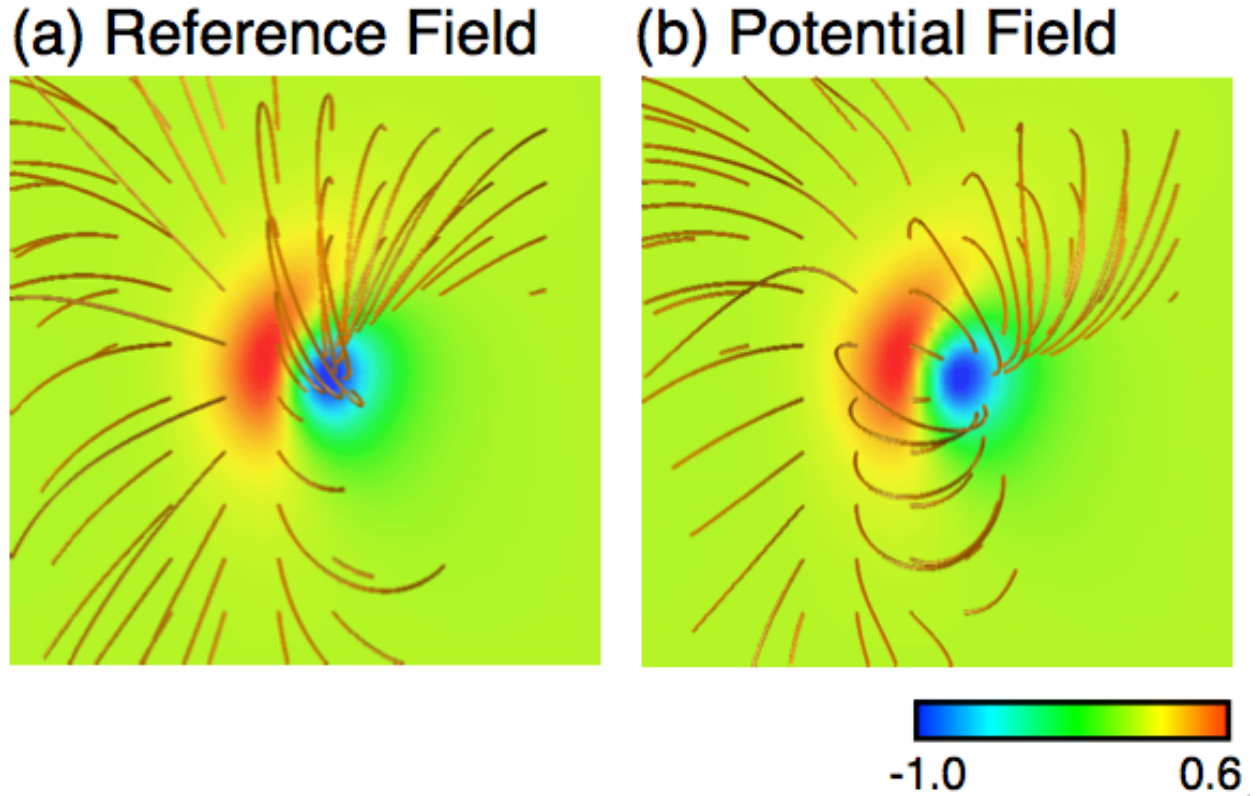


Fig. 1.— (a) Semi-analytical force-free solution introduced by Low & Lou (1990). Orange lines and color map represent magnetic field lines and distribution of normal component of magnetic field (B_z), respectively. (b) 3D field lines of potential field extrapolated from normal component of magnetic field on all the boundaries.

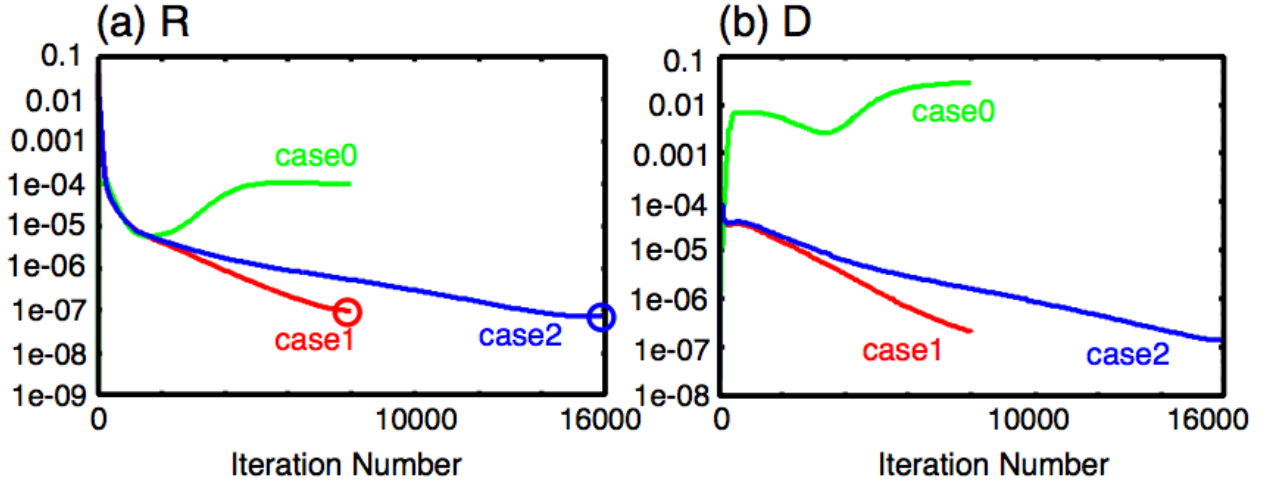


Fig. 2.— (a) Iteration profiles of $R = \int |\mathbf{J} \times \mathbf{B}|^2 dV$ for case0, case1, and case2 are plotted in green, red, and blue lines, respectively. Case0 and case1 use the EX type boundary condition, but case0 does not employ equation (6). Case2 uses the RW boundary condition. Red and blue circles indicate minimum values in case1 and case2. (b) Iteration profiles for $D = \int |\nabla \cdot \mathbf{B}|^2 dV$ for each case with same format as in (a).

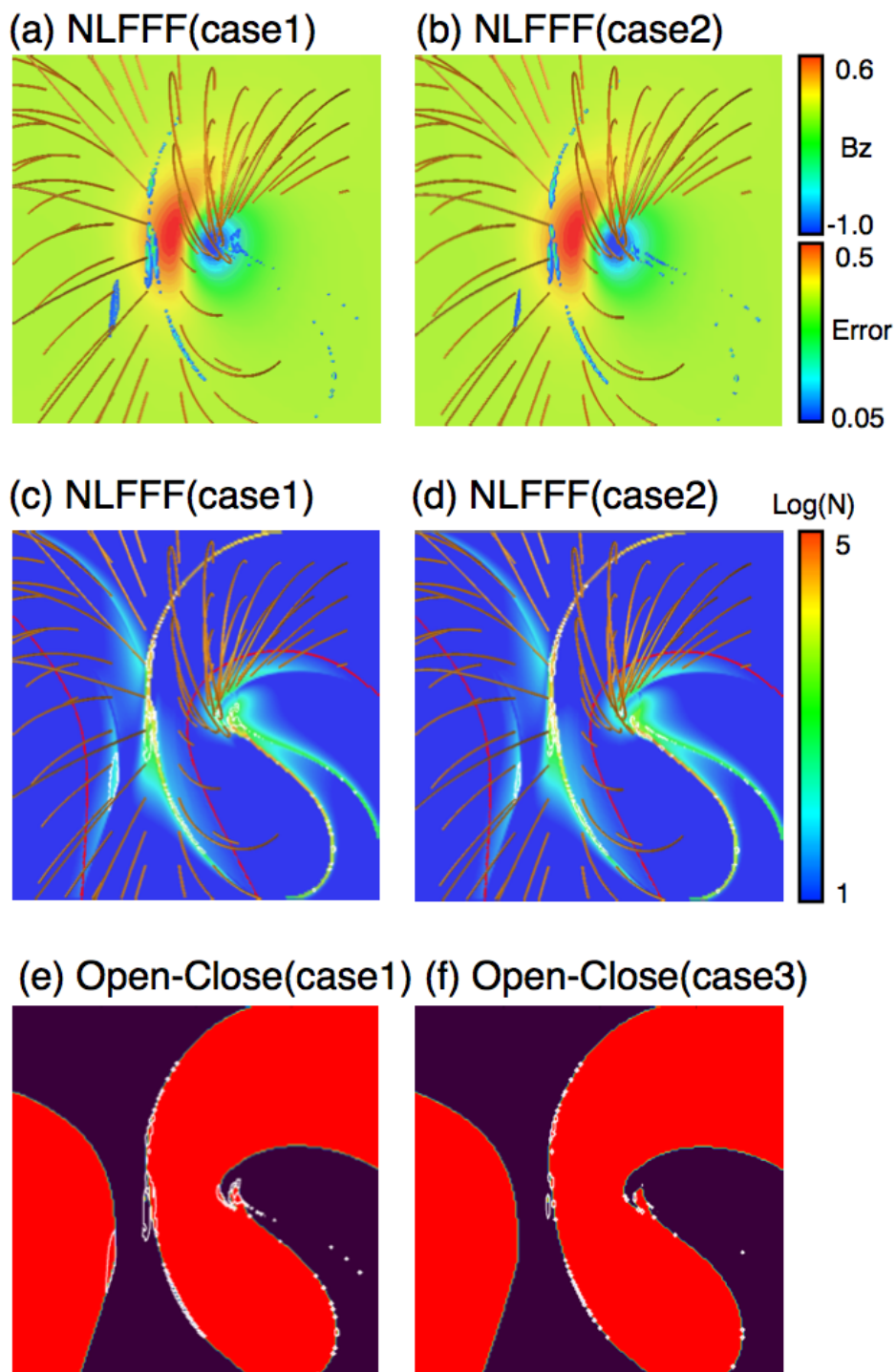


Fig. 3.— (a)-(b) 3D field lines of NLFFFs in case1 and case2. This format is the same as in Figure 1 except that the color contour represents the connectivity error defined in equation (11). (c)-(d) Field lines and connectivity errors (white contours with 0.05) plotted over the distribution of $\log(N)$, where N is defined in equation (12). (e)-(f) Connectivity errors in the same format as in (c) or (d) plotted over a map of the open-closed field lines in cases 1 and 3, respectively. Closed field line lie in red regions; other regions are occupied by open field lines.

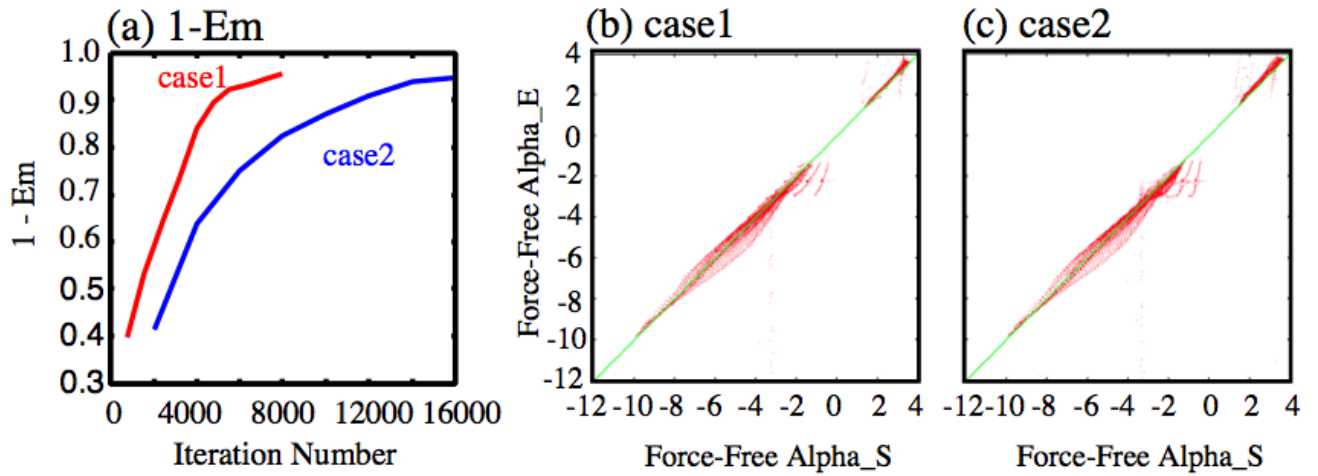


Fig. 4.— (a) Iteration profiles of $1 - E_m$ for case1 and case2 (red and blue lines, respectively), which are defined by equation (15). (b) Distribution of force-free α in case1. Horizontal and vertical axes represent the values of the force-free α at each footpoint of each field line. If this distribution is completely along the green line ($y = x$), the magnetic field completely satisfies a force-free state. (c) Distribution for case2 with same format as in (b).

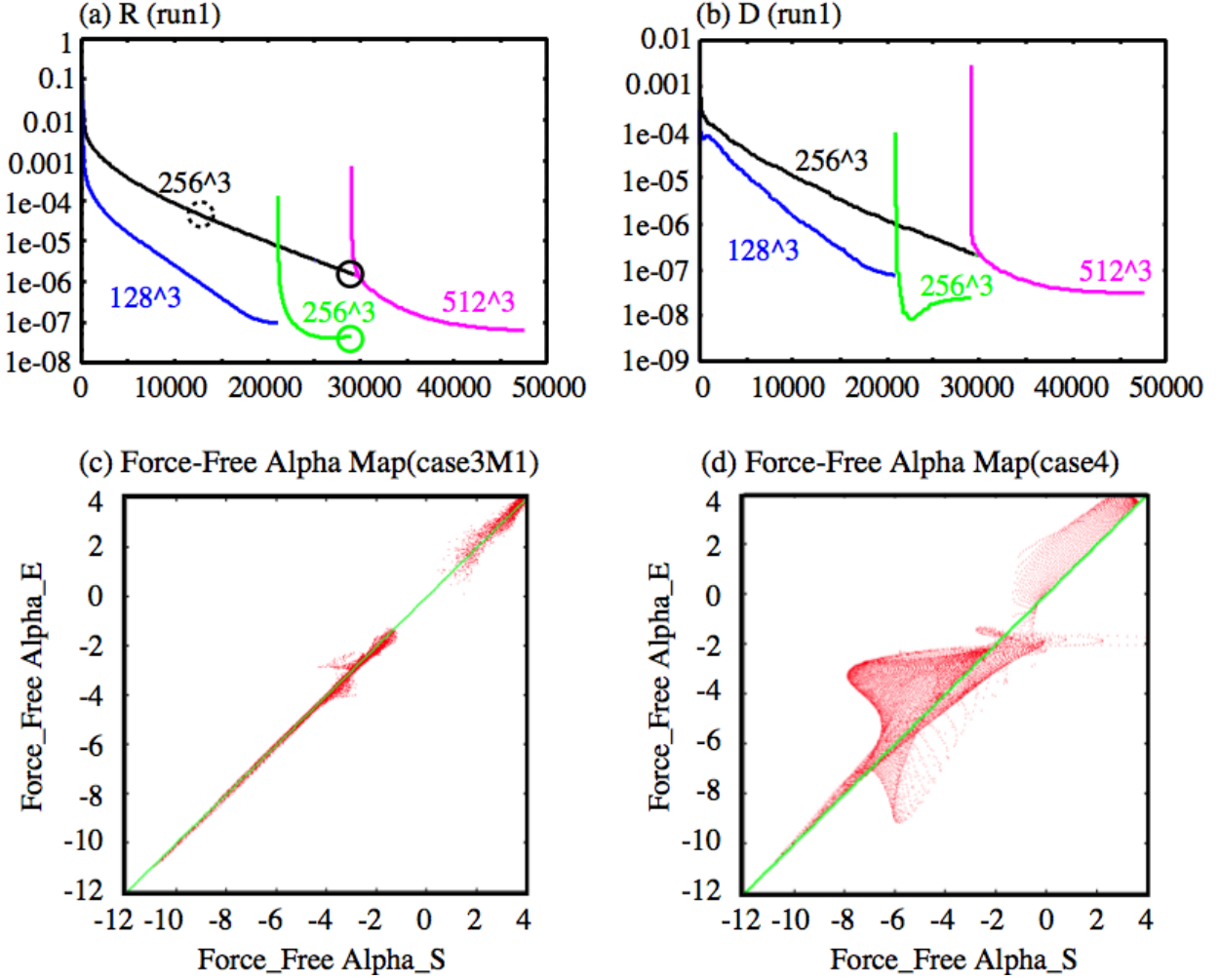


Fig. 5.— (a) Iteration profiles for $R = \int |\mathbf{J} \times \mathbf{B}|^2 dV$ in run1 using 128^3 (case3), 256^3 (case3M1), and 512^3 (case3M2) grid points, shown in the blue, green, and purple, respectively. Black line shows the result for case4, in which the multi-grid-type method is not applied and the number of grid points is fixed at 256^3 . Green and black solid circles show the end of the calculation using 256^3 grid points in case3M1 and case4, respectively; black dotted circle indicates the result of 12,500 iterations in case4, corresponding to the same calculation time with 3.0×10^4 iterations in case3M1 (green solid circle). (b) Iteration profiles for $D = \int |\nabla \cdot \mathbf{B}|^2 dV$ in run1 in same format in (a). (c) Distribution of force-free α obtained from case3M1, whose state is marked by the green circle in (a). Format is the same as in Figure 4. (d) Distribution of force-free α obtained for case4 after 12,500 iterations, marked by black dotted circle in (a).

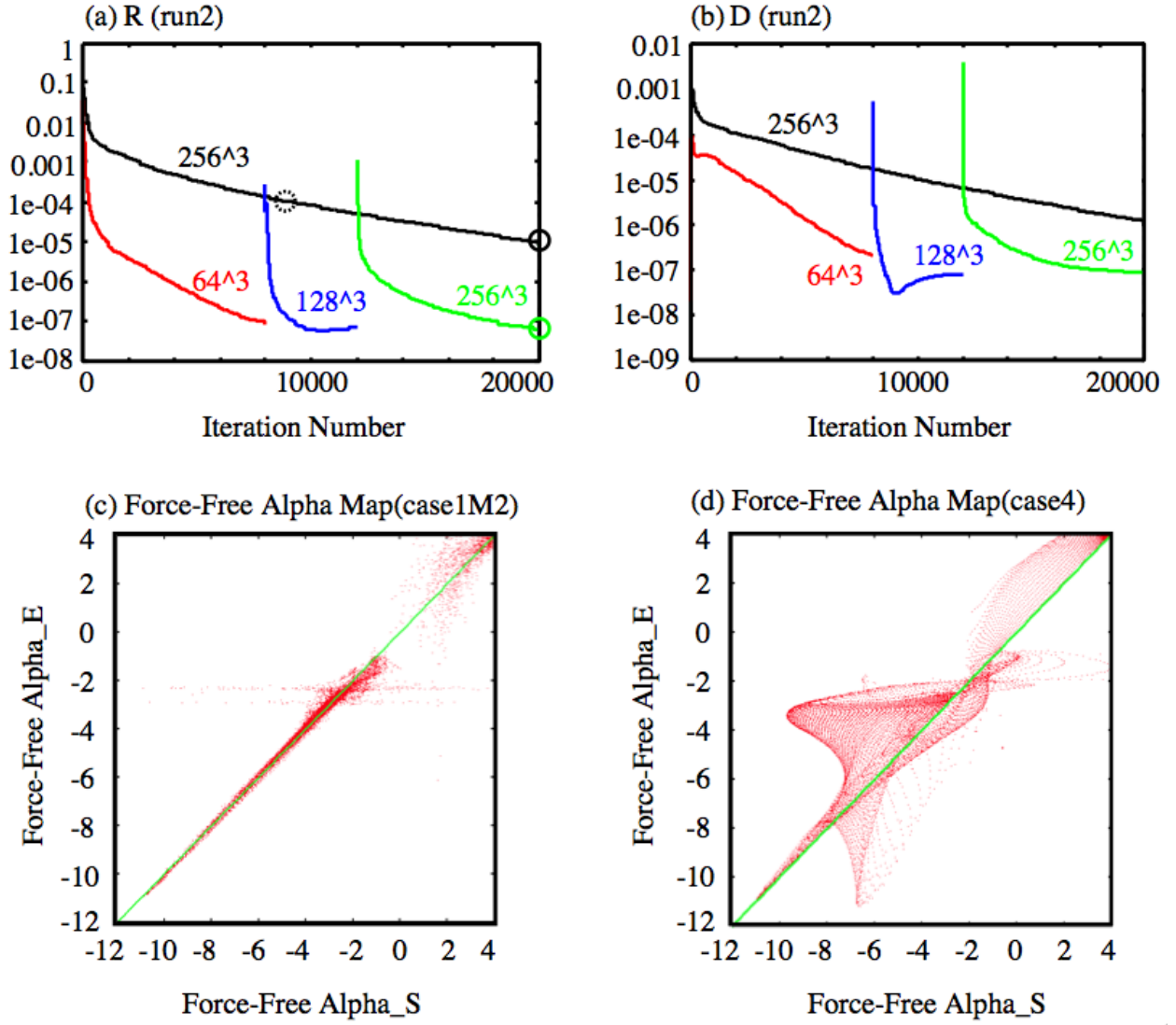


Fig. 6.— (a) Iteration profiles of $R = \int |\mathbf{J} \times \mathbf{B}|^2 dV$ in run2; format is essentially the same as in Figure.5(a). Initial grid number differs from that of run1 changing from 64^3 (case1, red) to 256^3 (case1M2, green) through 128^3 (case1M1, blue). Black line shows result for case4, which is the same as in Figure 5(a). Green and black solid circles represent 2.0×10^4 iterations for case1M2 and case4, corresponding to the end of calculation with 256^3 grid points. Black dotted circle represents 8625 iterations, corresponding to the same calculation time as at the end of case1M2. (b) Iteration profile of $D = \int |\nabla \cdot \mathbf{B}|^2 dV$ in run2. (c)-(d) Distributions of force-free α obtained from case1M2 and case4, marked by the green solid and black dotted circles in (a), respectively. These states are obtained in the same calculation time in each case.

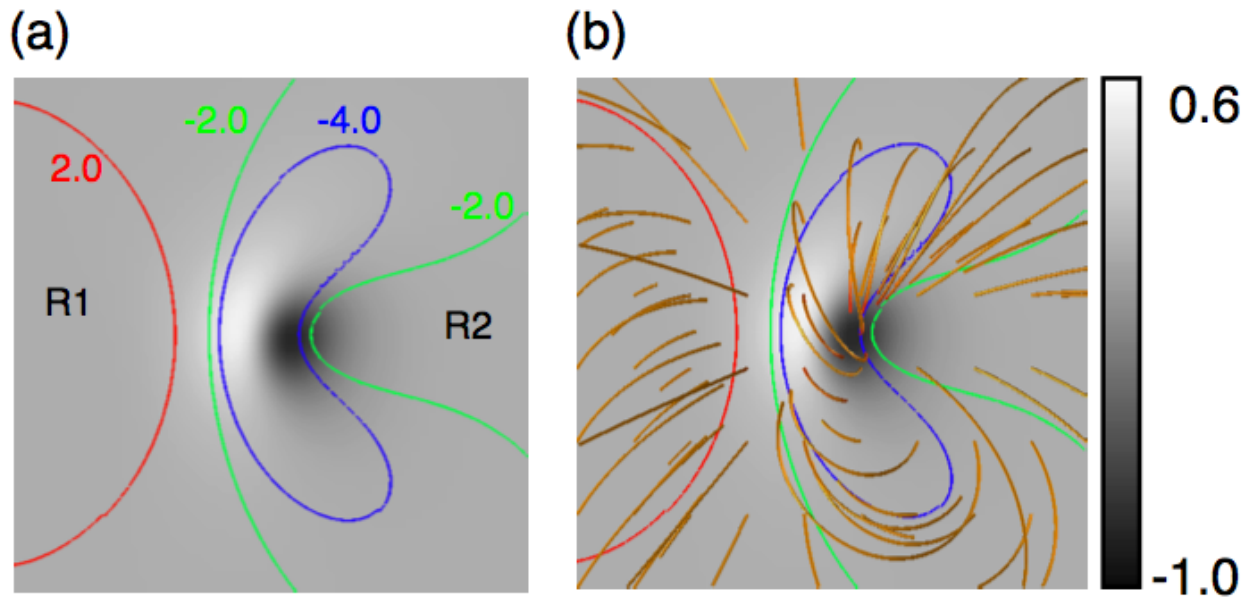


Fig. 7.— (a) Selected contours of the force-free α plotted over the B_z component in gray scale. Red, green, and blue lines represent the strengths 2.0, -2.0 , and -4.0 , respectively. R1 and R2, enclosed by the red and green lines, fall within $2.0 < \alpha < 4.0$ and $-2.0 < \alpha < 0$, respectively. (b) Magnetic field lines (orange lines) plotted over (a).

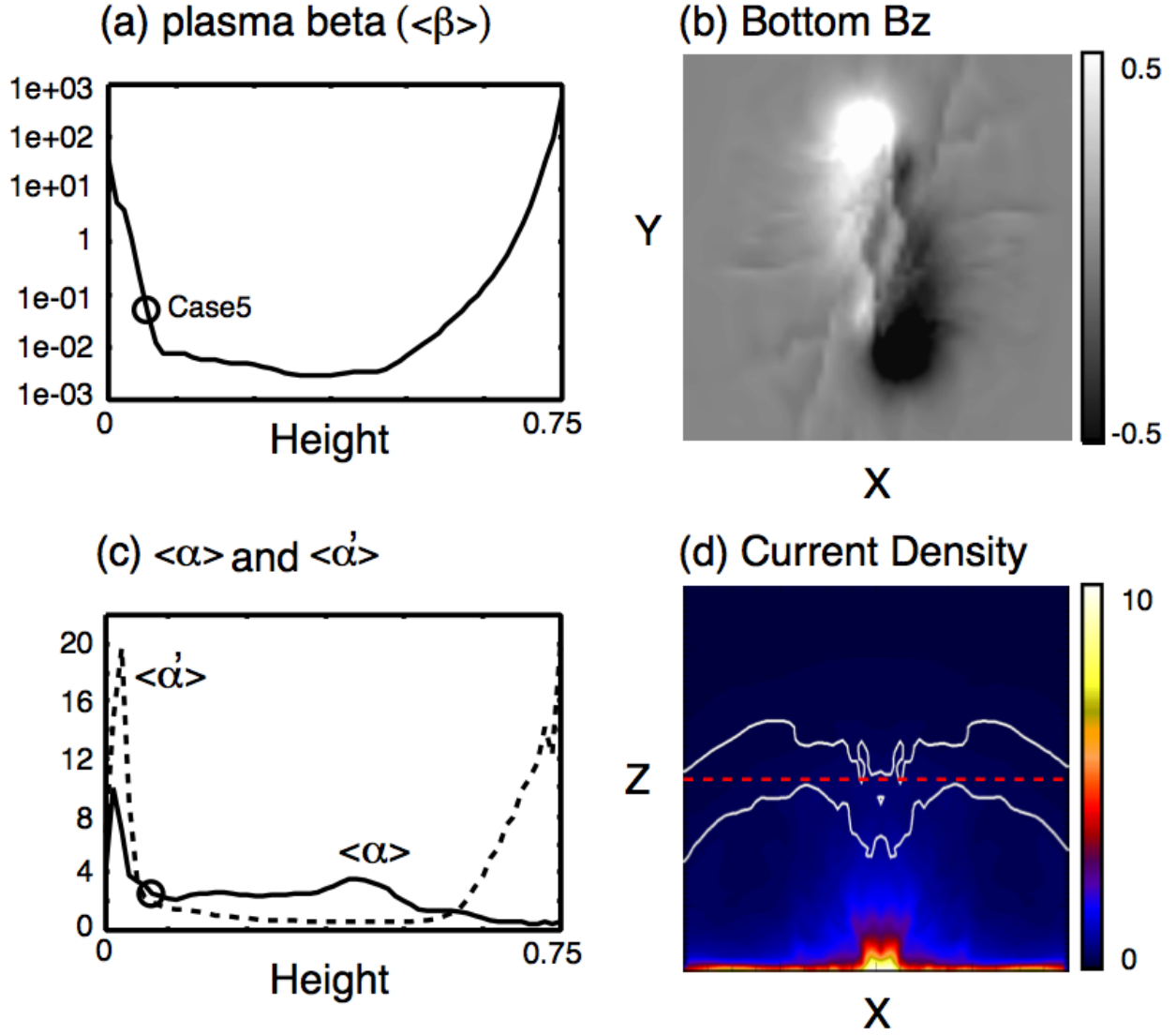


Fig. 8.— (a) Height profile of integrated plasma $\beta(\langle \beta(z) \rangle)$. Black circles indicate case5. (b) Distribution of B_z component at 2700 (km) above the photosphere plotted in gray scale, which is obtained from the flux-emergence simulation in the MT case in Magara (2012). This magnetic field is normalized by the maximum value($B_0=262(\text{G})$); *i.e.*, the maximum and minimum values correspond to 1 and -1 . (c) Height profiles of integrated force-free $\alpha \langle \alpha(z) \rangle$ (solid line) and non-force-free component $\langle \alpha(z)' \rangle$ (dashed line) according to the equations (18) and (19). (d) Velocity profile ($\int |\mathbf{v}| dy$) in white contours plotted over distribution of current density ($\int |\mathbf{J}| dy$). Strength of contours is 8.0. Red dotted line indicates half-height of entire domain.

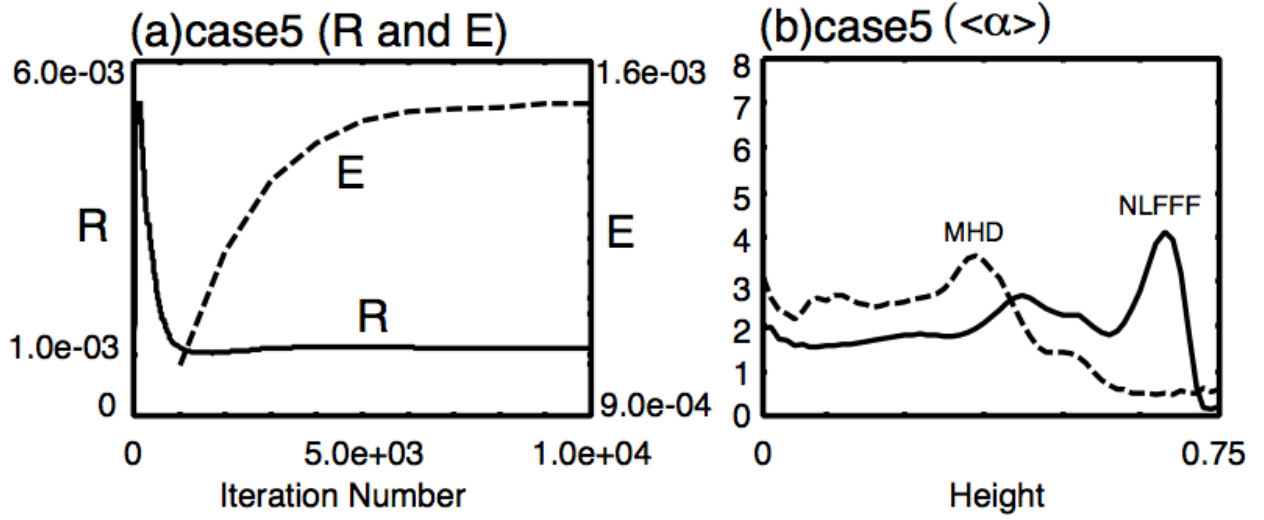


Fig. 9.— (a) Iteration profiles of total Lorentz force ($R = \int |\mathbf{J} \times \mathbf{B}|^2 dV$) and magnetic energy ($E = 1/2 \int |\mathbf{B}|^2 dV$) for case5. Solid and dashed lines represent R and E, the values of which are shown on the left and right vertical axes, respectively. (b) Height profile of integrated force-free α ($\langle \alpha \rangle$) calculated from MHD solution (dashed line) and $\langle \alpha_{nlfff} \rangle$ from NLFFF (solid line) in case5 calculated for $(0.25, 0.25) < (x, y) < (0.75, 0.75)$.

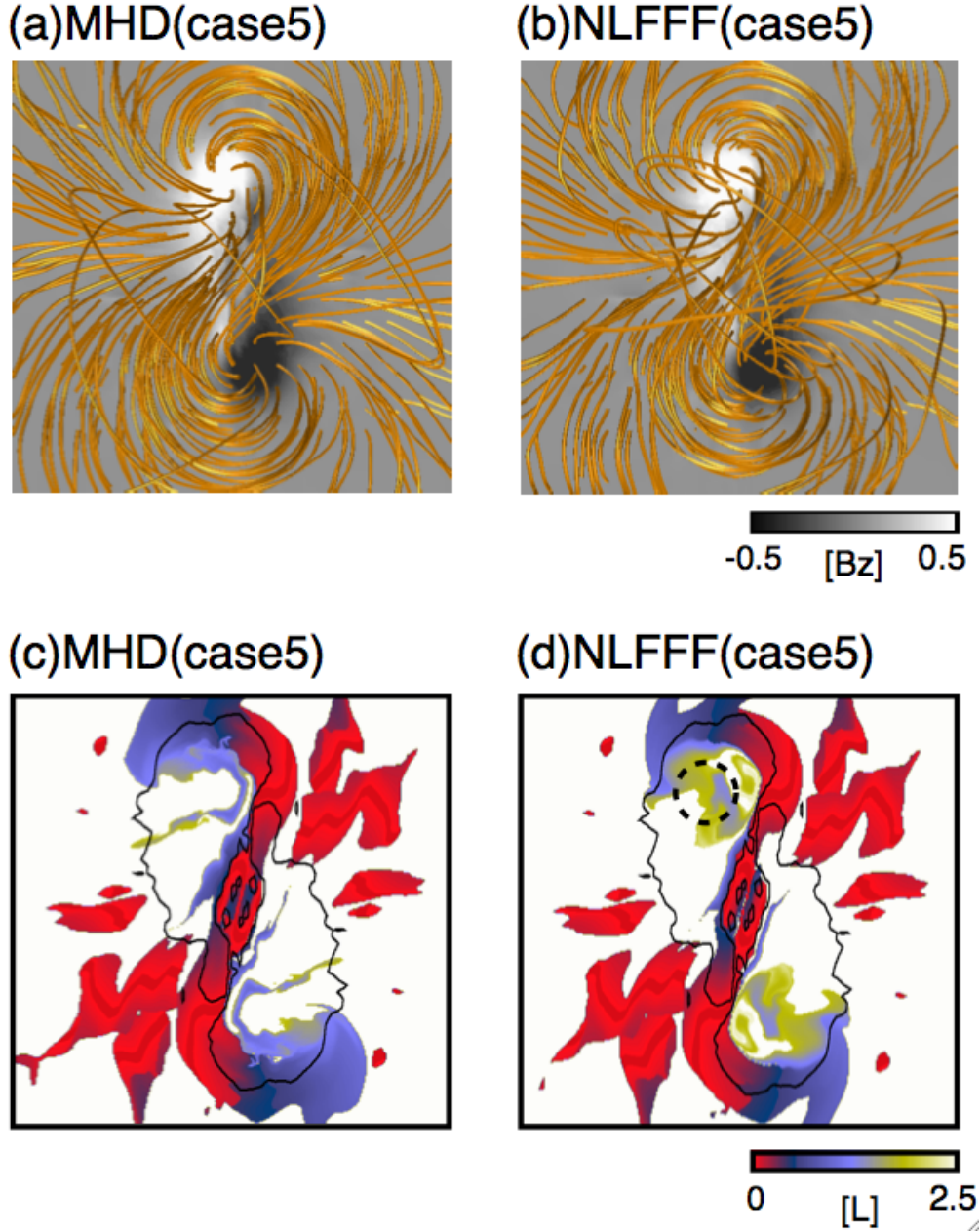


Fig. 10.— Selected field lines obtained using (a) MHD solution and (b) NLFFF in case5, plotted over the B_z component. Distribution of field line lengths mapped on the bottom surface obtained from (c) MHD solution and (d)NLFFF. All the field lines are traced from the bottom surface. Colored areas are occupied by closed field lines, both footpoints of which are anchored in the bottom surface, and whose maximum length is $L_{max} = 2.5$. White areas are dominated by another type of field lines with one footpoint rooted in the lateral boundaries. These are plotted in a range of $(0.1,0.1) < (x,y) < (0.9,0.9)$. Black solid lines represent a contour for the $|B_z| = 0.1$. Dashed circle marks region where closed loops are anchored.

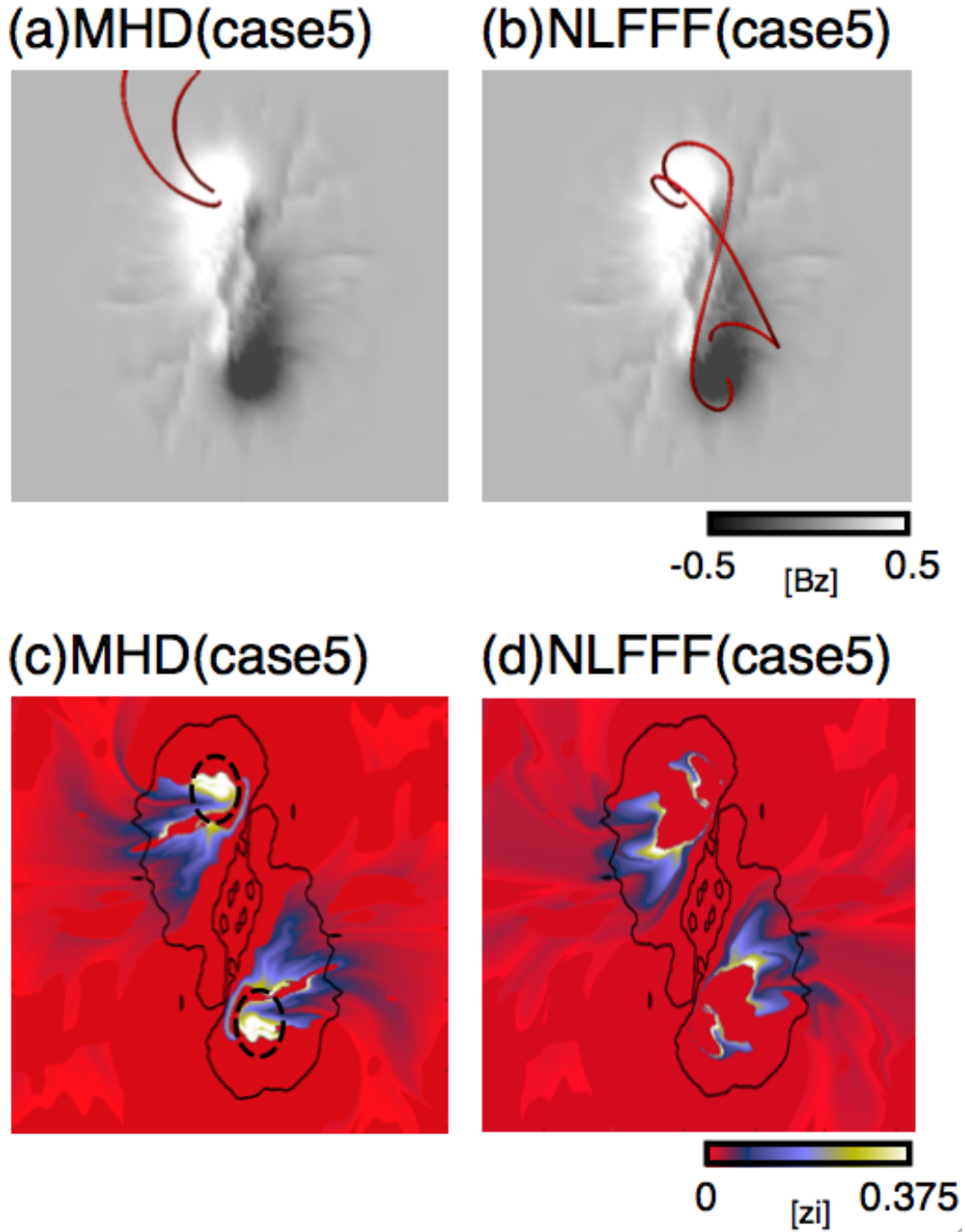


Fig. 11.— Selected field lines obtained using (a) MHD solution and (b) NLFFF for case5 traced from the dashed circle in Figure 10(d). The B_z component is plotted in gray scale in the same format as in Figure 8(b). Distribution maps of height of one footpoint in field line measured from bottom surface for (c) MHD solution and (d) NLFFF. Solid lines represent contours for $|B_z| = 0.1$.

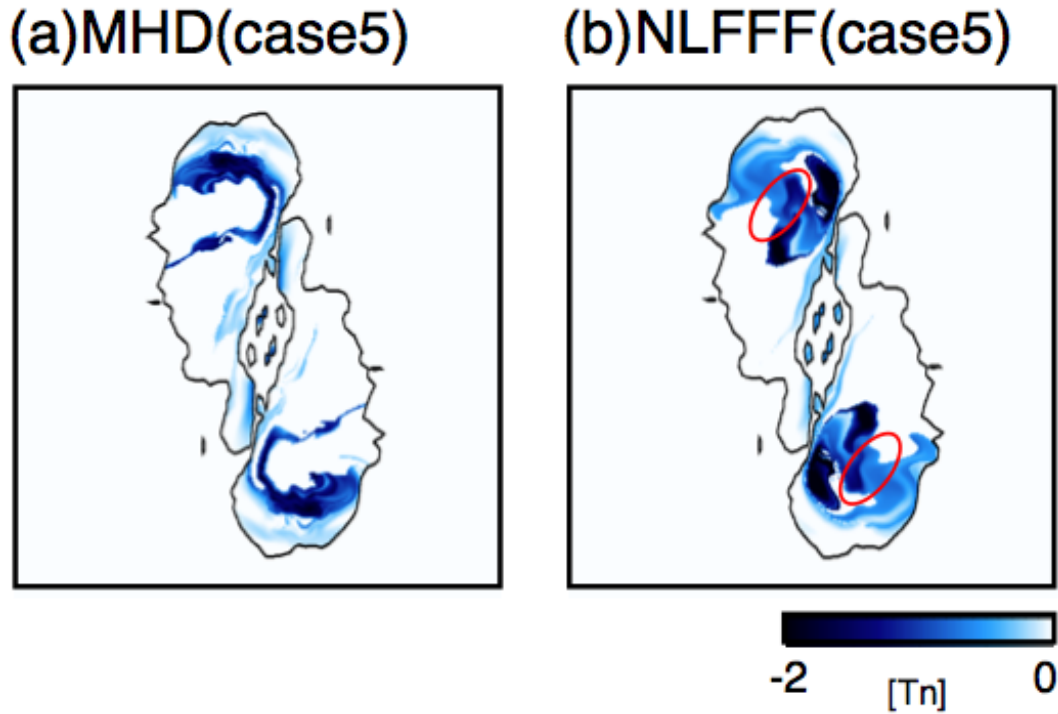


Fig. 12.— Twist value of each field line in (a) MHD solution and (b) NLFFF for case5 mapped on the bottom surface. B_z contours are plotted by solid lines ($|B_z| = 0.1$) in the same format as in Figures 10 or 11. The domain is set in the range of $(0.2,0.2) < (x,y) < (0.8,0.8)$.

Table 1: These are parameters in all cases.

Parameters	BC	R_{min}	v_{max}	c_h	η_0	$d\gamma$	GN
case1	EX	1.0×10^{-4}	1.0	5.0	3.75×10^{-5}	-	64^3
case1M1	EX	1.0×10^{-4}	1.0	5.0	0	-	128^3
case1M2	EX	1.0×10^{-4}	1.0	5.0	0	-	256^3
case2	RW	1.0×10^{-4}	1.0	5.0	3.75×10^{-5}	-	64^3
case3	EX	1.0×10^{-4}	1.0	5.0	3.75×10^{-5}	-	128^3
case3M1	EX	1.0×10^{-4}	1.0	5.0	0	-	256^3
case3M2	EX	1.0×10^{-4}	1.0	5.0	0	-	512^3
case4	EX	1.0×10^{-4}	1.0	5.0	3.75×10^{-5}	-	256^3
case5	RW	5.0×10^{-3}	5.0×10^{-2}	0.2	5.0×10^{-5}	0.02	$80 \times 80 \times 60$

Table 2: The result of the quantitative analysis, introduced by Schrijver et al. (2006), for Low & Lou solution.

Star	method	C_{vec}	C_{cs}	$1 - E_N$	$1 - E_M$	ϵ	grid number
Low & Lou	-	1.00	1.00	1.00	1.00	1.00	64^3
Wiegelmann	Optimization	1.00	1.00	0.98	0.98	1.02	64^3
case1	MHD Relaxation	1.00	1.00	0.97	0.95	1.02	64^3
case2	MHD Relaxation	1.00	1.00	0.97	0.95	1.04	64^3
case3	MHD Relaxation	1.00	1.00	0.99	0.98	1.00	128^3
case4	MHD Relaxation	1.00	1.00	0.98	0.96	0.99	256^3
case1M1	MHD Relaxation	1.00	1.00	0.97	0.94	1.02	128^3
case1M2	MHD Relaxation	1.00	1.00	0.97	0.93	1.02	256^3